minerals

MDPI

Article

Characteristics of Naturally Formed Nanoparticles in Various Media and Their Prospecting Significance in Chaihulanzi Deposit

Meiqu Lu [1,2,3,4], Jianjin Cao [1,2,3,4,*], Zhengyang Wang [1,2,3,4] and Guoqiang Wang [1,2,3,4]

1 School of Earth Sciences and Engineering, Sun Yat-sen University, Guangzhou 510275, China
2 Guangdong Provincial Key Laboratory of Mineral Resources and Geological Processes, School of Earth Sciences and Engineering, Sun Yat-sen University, Guangzhou 510275, China
3 Guangdong Provincial Key Laboratory of Geodynamics and Geohazards, School of Earth Sciences and Engineering, Sun Yat-sen University, Guangzhou 510275, China
4 Southern Marine Science and Engineering Guangdong Laboratory (Zhuhai), Zhuhai 519000, China
* Correspondence: eescjj@mail.sysu.edu.cn

Abstract: In recent years, the exploration of concealed deposits has become extremely urgent as the shortage of surface resources worsens. In this study, naturally formed nanoparticles in five media (deep-seated fault gouge, ascending gas flow, soil, shallow groundwater and deep groundwater) in Chaihulanzi Au deposit, China, were analyzed by transmission electron microscopy. The characteristics of category, shape, lattice parameters, chemical component and association were obtained. The results show that deep media can carry natural nanoparticles to the surface media, resulting in an increased proportion of O and metal chemical valence such as Pb and Cu in nanoparticles. The metal elements Au, Ag, Cu, Zn and As in nanoparticles correspond to those of orebody minerals. Au-Ag-Cu, Fe-As, Cu-Sn and Pb-Zn element associations in nanoparticles are similar to those of mineral composition or orebody paragenesis in Chaihulanzi deposit. Compared with nanoparticle characteristics in deposit and background areas, it can be deduced that natural ore-bearing nanoparticles come from concealed orebodies. With the characteristics of more oxide forms and the dislocation of the crystal lattice, these nanoparticles are formed by faulting and oxidation. Nanoparticles produced in concealed orebodies that migrate from the deep to the surface media could be used for prospecting.

Keywords: Chaihulanzi Au deposit; nanoparticles; concealed deposit; prospecting

Citation: Lu, M.; Cao, J.; Wang, Z.; Wang, G. Characteristics of Naturally Formed Nanoparticles in Various Media and Their Prospecting Significance in Chaihulanzi Deposit. *Minerals* **2022**, *12*, 1289. https://doi.org/10.3390/min12101289

Academic Editor: Athanasios Godelitsas

Received: 5 September 2022
Accepted: 11 October 2022
Published: 13 October 2022

1. Introduction

With the increasing shortage of mineral resources, the exploration of concealed deposits has become a research hotspot among geoscientists around the world. Geophysical and geochemical exploration are the main technical methods for the exploration of concealed orebodies. There are geochemical exploration methods, such as the geogas [1–7], enzyme leach [8,9], electro [10–13] and mobile metal ion [14–17] methods. Among these geochemical exploration methods, the geogas exploration method has been in use for only a few decades, being used to prospect concealed orebodies by analyzing the element content in geogas via such measures as neutron activation, atomic absorption and ICP-MS [1,2,18,19]. Geogas mainly consists of N_2, O_2, CO_2, CO, CH_4 and NH_3 [3], originating from the degassing of the upper mantle and lithosphere [20–24]. Nanoscale particles have been observed in geogas [25], but other details of the nanoparticles in geogas remain to be excavated.

Cao et al. [26–28] first proposed a technique for prospecting concealed orebodies based on the characteristics of natural nanoparticles. Au, $PbSO_4$ and WO_3 nanoparticles in the ascending gas flow above the Changken gold deposit, China, were found that could be used for prospecting [26]. Since then, further studies have been conducted,

analyzing the characteristics of nanoparticles in groundwater [29–34], fault gouges [35,36], ascending gas flows [37–41] and animals and plants [42–44], obtaining information on concealed orebodies.

In this study, the natural single-nanoparticle analysis technique of transmission electron microscopy (TEM) is used to observe nanoparticles in five media (deep-seated fault gouge, ascending gas flow, soil, shallow groundwater and deep groundwater), including their morphology, element association, nanostructure and crystalline characteristics. The main purposes of this study are as follows: (1) to compare the similarities and differences of natural nanoparticles in five media, (2) to explain the relationship between natural nanoparticles in deep and shallow media, namely deep and shallow groundwater samples, as well as deep fault gouge and soil samples, and (3) to analyze the provenance of ore-bearing nanoparticles in these five media. More importantly, this study attempts to study the formation and migration of different kinds of natural metal-bearing (especially ore-forming elements) nanoparticles in different media, and provides a new basis for studies on prospecting nanoparticles.

2. Geological Setting

The Chaihulanzi gold deposit is located 40 km west of Chifeng City, Inner Mongolia, China (Figure 1). It is situated in the western part of the Chifeng-Chaoyang metallogenic belt of the northern margin of North Chian Craton (NCC), which is an important gold mining district in China [45–52]. Metallic deposits in this area include Au-Cu, Mo-Cu, Pb-Zn, Cr and Fe [52–56].

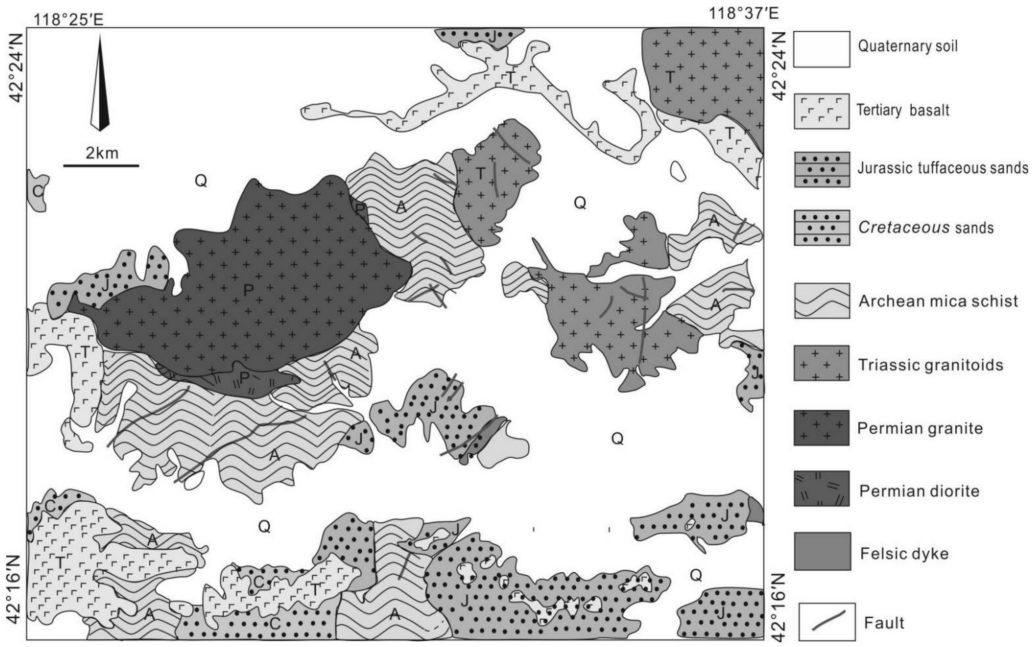

Figure 1. Regional geologic map of Chaihulanzi deposit (Modified by [48,57]).

The main overburden of the Chaihulanzi deposit is quaternary loess soil. Precambrian metamorphic rocks are exposed and the orebodies are mainly hosted in the gneiss (Figure 2) [57]. The local outcropping lithologies predominantly include granitoid and dioritoid rocks. The ore types of this deposit are mainly pyritization-altered rock and quartz-vein-type ore, and the average gold grade is 5.48 g/t (as provided by the Chaihulanzi Mine Group). Chaihulanzi deposit is a hydrothermal deposit [45,46]. Ore minerals in this deposit include primarily pyrite, natural gold, chalcopyrite, galena, sphalerite, hematite and magnetite, with a limited amount of galenobismutite and native silver, while gangue minerals are predominantly quartz, calcite, chlorite, sericite and garnet [47,57]. Additionally, orebodies are found in the NW–SE vein extension at a depth of 150 to 500 m.

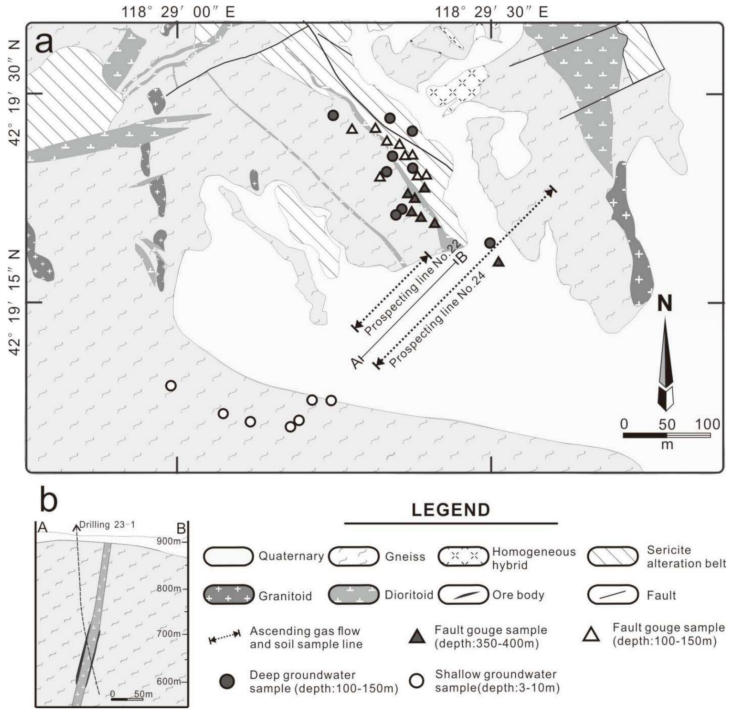

Figure 2. (**a**) Detailed geological map and (**b**) cross-section of the Chaihulanzi gold deposits. (Modified by [57]).

This deposit is seated in the middle and low mountainous area of the northern foot of Yanshan Mountains at an altitude of 850 to 1200 m. Being far away from the ocean, the deposit area belongs to a semi-arid continental climate zone. The only source of groundwater recharge in bedrock fissures is the infiltration of atmospheric precipitation. Aquifers are generally bedrock fissure aquifers, which are composed of weathered bedrock fissure water and vein-like structural fissure water.

3. Sampling and Analytical Methods

Sampling plan and details of samples were shown in Table 1.

Table 1. The sampling plan and details of samples.

Sampling Type	Sample Quantity	Number of Observed Particles	Particle ID	pH	Depth (m)	Location
Deep-seated fault gouge	17	49	1–7	-	100–150 and 350–400 m	Deep-seated mine (Chaihulanzi deposit)
Ascending gas flow	36	147	8–13	-	Surface	Prospecting lines 22 and 24 (Chaihulanzi deposit)
Soil	36	133	14–19	-	0.8	Prospecting lines 22 and 24 (Chaihulanzi deposit)
Shallow groundwater	7	26	20–23	7.73–8.36	3–10	Water wells in southwest of the deposit
Deep groundwater	9	28	24–27	7.76–8.26	100–150	Deep-seated mine (Chaihulanzi deposit)
Background ascending gas flow	5	13	B1–B4	-	Surface	Yangbadi village
Background soil	5	40	B5–B8	-	0.8	Yangbadi village

3.1. Deep-Seated Fault Gouge Samples

Deep-seated fault gouge samples were collected from the fracture zone of the deep mining roadway in the Chaihulanzi Au deposit. A 100 g fault gouge sample was obtained at each sampling site. Prior to sampling, the surface of the fault gouge should be carefully removed to avoid the effect of dust. The preparation method for obtaining natural nanoparticles in fault gouge samples for analysis by TEM has been clearly described in previous studies [40,58,59]. Briefly, the fault gouge samples were dried for 24 h at 50° in a constant-temperature oven. Additionally, each dried fault gouge sample was screened with 80 mesh. Then, the fault gouge powders were placed in a beaker and gently blown to raise dust with a washing ear ball. The TEM grid was suspended in the container to absorb nanoparticles for 5–10 min.

3.2. Ascending Gas Flow and Soil Samples

Ascending gas flow samples were collected near the No.22 and No.24 prospecting lines, where the orebodies are highly concentrated and exhibit large thicknesses. The sampling devices with carbon-coated nickel TEM grids were buried 80 cm under the surface (Figure 3) [40,58,59]. In this device, the TEM grid was fixed on plastic pipe with two nylon meshes and then embedded within a 100 cm-long steel pipe with assistance from a silica gel plug. In order to absorb more natural nanoparticles, the carbon-containing film side of the TEM grid was placed face down. Finally, a plastic cup was used to cover a leak of the steel pipe to prevent the effect of pollution and atmospheric rainfall. The TEM grids were recovered after 45 days, and then placed in a dry and sealed sample box. Soil samples were collected in the same sampling sites as ascending gas flow samples. A 100 g soil sample was collected from a depth of 80 cm below the surface at each sampling site. The preparation process of soil for TEM analysis was the same as that for the fault gouges sample.

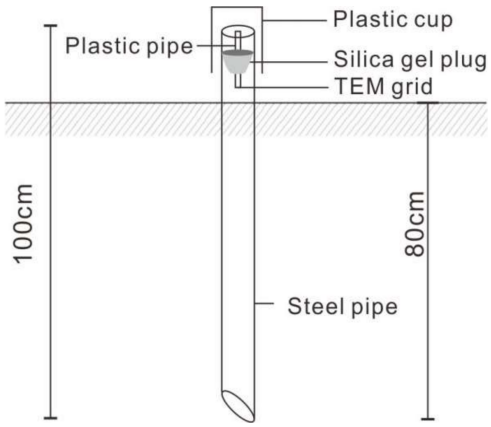

Figure 3. Sketch of the collector for nanoparticles carried by ascending gas flow.

The Yangbadi village, the Nei Monggol Autonomous Region (China), 10 km away from the Chaihulanzi deposit was selected as a background study area. Its geological background (including overburden, magmatic rocks and tectonic structure) is similar to that of the Chaihulanzi deposit. Moreover, there is no industrial or living pollution, such as mining and wastewater discharge. The sampling and analytical methods used were same as those used for samples collected in the deposit area.

3.3. Shallow and Deep Groundwater Samples

The shallow groundwater samples were collected in drinking water wells southwest of the Chaihulanzi gold deposit. To collect water, 500 mL PE bottles were used, which were washed with high-purity water before sampling three times. The pH values were tested in situ, and were found to range from 7.73 to 8.36. Deep groundwater samples were collected in level No.2 of the vertical shaft and No.1 of the deposit, at a depth of nearly

100–150 m. In the same manner as for the shallow groundwater, 500 mL PE bottles were used to collect the deep groundwater that seeped from the rock fissures. The pH values ranged from 7.76 to 8.26 in situ. Before TEM analysis, nanoparticles in water samples were transferred onto carbon-coated nickel grids, the details of which were given in a previous study [31,33]. The method for obtaining nanoparticles in shallow and deep groundwater samples was the same, including shaking, transference and drying.

3.4. TEM Analysis

The nanoparticles were observed by TEM at the Testing Center of Yangzhou University (Tecnai G2 F30 S-TWIN, America) and the Testing Center of Suzhou University (Tecnai G220, 200 kV America). The Tecnai G2 F30 S-TWIN has a 50–300 kV accelerating voltage, 0.20 nm point resolution, 0.102 nm line resolution and 60–1000 kx magnification. The Tecnai G220 has a maximum accelerating voltage of 20–200 kV, 0.24 nm point resolution, 0.14 nm line resolution and 25–1030 kx magnification. During characterization process, both them use their highest acceleration voltages (Tecnai G2 F30: 300 kV; Tecnai G220: 200 kV) to ensure the best resolving ability. Energy dispersive spectroscopy (EDS) was used to characterize the element composition of the nanoparticles. The crystalline features of the nanoparticles were identified by selected area electron diffraction (SAED). High-resolution TEM (HRTEM) was used to observe the nanostructure of nanoparticles, including lattice fringes and lattice spacing. The EDS dates were analyzed by TEM Imagine & Analysis (TIA) software. Additionally, the Digital Micrograph (DM) software was used to obtain some detailed information, including the SAED pattern and HRTEM image. All of this information should be considered for phase analysis, using a reference from jade6 software with a 2009 standard Powder Diffraction File (PDF) card. EDS analysis can be affected by the material of the TEM grids. Because the grids used in this study were made of carbon-coated nickel, the concentrations of nickel (Ni) and carbon (C) were eliminated in the EDS analyses.

4. Results

This study focuses on the analysis of metal-bearing particles, especially ore-bearing nanoparticles. According to the TEM analysis, the characteristics of nanoparticles in various types of samples were summarized, and the typical nanoparticles were analyzed and described in detail.

4.1. Nanoparticles in Deep-Seated Fault Gouges

In fault gouge samples, a natural single gold-bearing nanoparticle (ID1) with irregular shape and uneven contrast with a size of 150 × 80 nm^2 (Figure 4a) was found, and is shown in Figure 4. The EDS spectrum shows that the peaks of Au are obviously high, followed by O, Cu, Mg and Na, respectively (Figure 4d), in addition to the higher level of Ni in the nickel grid. Diffraction spots in the SAED pattern show that the nanoparticle is crystalline, two of which spots were calculated to have interplanar d-spacings of 1.6 and 2.5 Å (Figure 4b). Clear lattice fringes can be seen in the HRTEM image (Figure 4c). One of the interplanar d-spacings, 10d = 2.5 nm (d = 2.5 Å), is given in the HRTEM image (Figure 4c). Combined with the EDS results, these d-spacings (d = 1.6 Å, 2.5 Å, 2.5 Å) correspond to interplanar d-spacings of Cu oxide (PDF#49-1830) of (323), (202), (202). Therefore, this nanoparticle may contain native gold and Cu oxides. A large number of natural Fe-bearing nanoparticles could be observed, usually containing As. Figure 5a shows an Fe-, As- and Pb-bearing aggregation (ID2) with a size of 150 × 100 nm^2. Its SAED pattern shows that it is amorphous without any diffraction spots. According to the EDS result (Table 2), it mainly consists of Fe oxides.

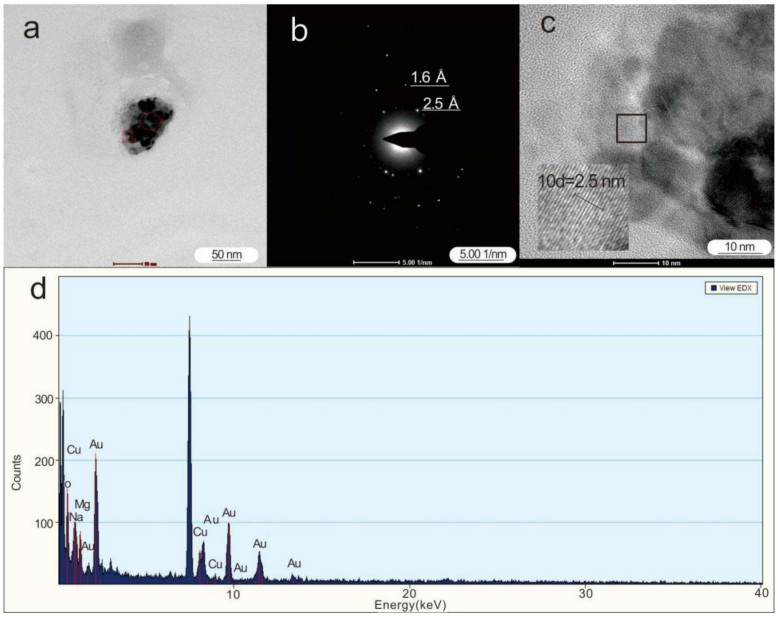

Figure 4. (**a**) TEM photomicrographs, (**b**) SAED pattern, (**c**) HRTEM image and (**d**) EDS spectrum of Au-, Cu-bearing nanoparticle carried by the deep-seated fault gouge (ID1).

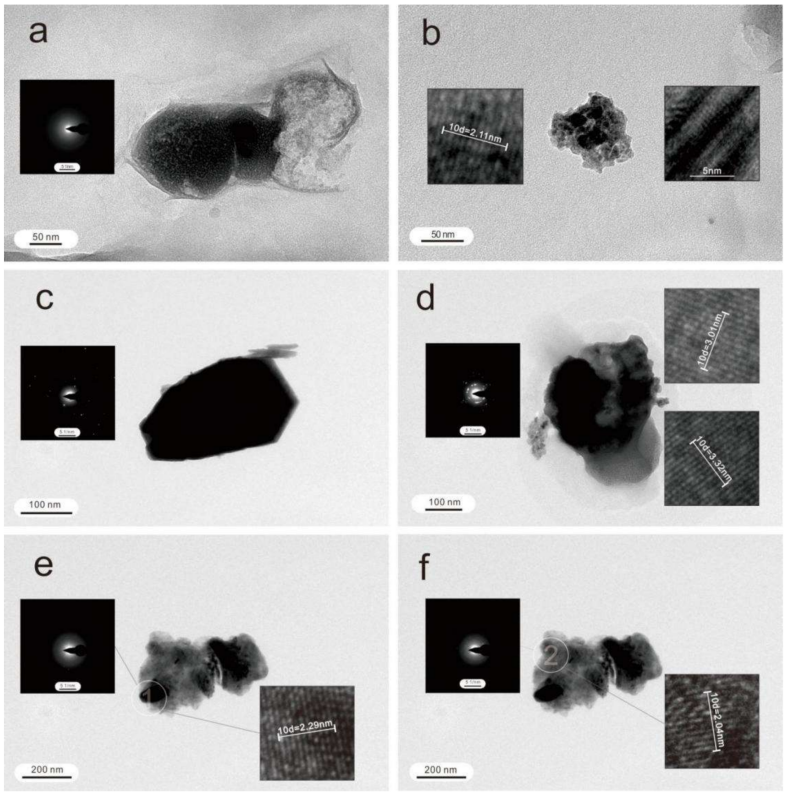

Figure 5. TEM photomicrographs of particles or aggregations in the deep-seated fault gouges. (**a**) TEM image and SAED pattern of an Fe-, As- and Pb-bearing aggregation (ID2). (**b**) TEM image and HRTEM images of a Cu-bearing particle aggregation (ID3). (**c**) TEM image and SAED pattern of a Zn-bearing particle (ID4). (**d**) TEM image, SAED pattern and HRTEM images of a Pb, Zn, As, Fe, and Cu-bearing particle (ID5). (**e**,**f**) TEM image of a multiple-metal-bearing aggregation. (**e**) SAED pattern and HRTEM image of position 1(ID6). (**f**) SAED pattern and HRTEM image of position 2 (ID7).

Table 2. The EDS data of particles and particle aggregations in deep-seated fault gouge (ID1-7) and ascending gas flow (ID8-13).

Particle ID	Elements (%)	Au	O	Na	Mg	Al	Si	S	Cl	K	Ca	V	Cr	Mn	Fe	Co	Cu	Zn	Mo	Sn	Pt	Pb	Bi	As	F	Size/nm^2
1	wt%	74.0	12.5	2.8	3.1												7.6									150 × 80
	at%	24.6	51.15	8.0	8.4												7.8									
2	wt%		47.0		1.3	2.6	4.3	0.6			2.3			0.4	31.0							7.8		2.7		150 × 100
	at%		74.3		1.4	2.5	3.8	0.4			1.5			0.2	14.0							0.9		0.9		
3	wt%		17.4			1.9	1.8	3.7		3.0	2.0			0.3	2.4		63.7								3.6	70 × 50
	at%		40.2			2.6	2.4	4.3		2.8	1.9			0.2	1.6		37.0								7.0	
4	wt%		11.8	19.0											0.7	0.5		68.0								200 × 350
	at%		28.1	31.4											0.5	0.3		39.6								
5	wt%		9.5						5.5						1.4		6.3	9.2		3.8		54.1		10.2		300 × 350
	at%		41.3						10.7						1.8		6.9	9.7		2.2		18.1		9.4		
6	wt%		19.5		0.8	0.7	0.9	9.1			1.4				1.0		37.2						28.0		1.5	250 × 350
	at%		50.0		1.3	1.1	1.3	11.6			1.4				0.7		23.9						5.5		3.2	
7	wt%		61.0	5.0	1.7	1.1	3.7	6.7	1.6	0.8	7.5				2.5		6.8		1.6							250 × 350
	at%		77.7	4.5	1.4	0.8	2.7	4.3	0.9	0.4	3.8				0.9		2.2		0.3							
8	wt%		54.4										1.2	1.3	43.1											30 × 150
	at%		80.6										0.6	0.6	18.3											
9	wt%		20.8												0.4		61.1				17.7					60 × 70
	at%		55.2												0.3		40.7				3.8					
10	wt%		22.3				2.60										65.9			9.2						100 × 200
	at%		53.6				3.60										39.8			3.0						
11	wt%		67.2				5.50											19.0				8.3				50 × 150
	at%		88.8				4.20											6.2				0.8				
12	wt%		20.0	11.2	1.5				2.8	4.1	7.80	4.9			0.8		14.2	1.8					30.7			50 × 250
	at%		46.4	18.2	2.3				3.0	3.9	7.20	3.6			0.5		8.3	1.0					5.5			
13	wt%		57.3		1.4				28.2	4.4								3.3	5.4							100 × 200
	at%		77.0		1.2				17.1	2.4								1.1	1.2							

Generally, natural Cu-bearing nanoparticles (or aggregation) exist in form of Cu oxide nanoparticles. Figure 5b shows a Cu-bearing aggregation (ID3) with a size of 70 × 50 nm^2. The HRTEM image shows an aggregation with crystalline features. The composition of the aggregation contains of O (17.4%) and Cu (63.7%) (Table 2), suggesting that the aggregation mainly consists of Cu oxide. A natural single Zn-bearing nanoparticle (ID4) is shown in Figure 5c. The shape of this nanoparticle clearly shows three sides of the hexagon in the TEM image. There are several diffraction spots in the SAED pattern, showing that it is crystalline. It contains O (11.8%), Na (19.0%), and Zn (68.0%) (Table 2), suggesting that this natural single nanoparticle consists of Zn oxide and sodium carbonate.

The natural aggregations, containing a variety of metal elements, are commonly observed in deep-seated fault gouge samples. Figure 5d shows a natural single nanoparticle (ID5) containing metal elements, including Pb, Zn, As, Fe, Cu and Sn (Table 2). Besides metal elements, it also contains O and Cl. The SAED pattern shows that it is polycrystalline with regular diffraction spots. In the HRTEM image, two crystalline interplanar d-spacings are measured as 3.01 Å (10d = 3.01 nm) and 3.32 Å (10d = 3.32 nm), which are similar to those of the (−212), (200) lattice plane d-spacing of Pb_2O_3 (PDF#23-0331) in the standard PDF card, indicating that it mainly contains Pb_2O_3.

Figure 5e,f show a natural aggregation with a size of 200 × 300 nm^2, and the position 1 (ID6) and position 2 (ID7) of this aggregation are analyzed in detail. Position 1 (Figure 5e) had high contrast, mainly consisting of Cu (37.2%), Bi (28.0%), O (19.5%), S (9.1%) and a small amount of Ca, Mg, Al, Si, Fe and F. According to the EDS results (Table 2), the atomic ratio of S and O was nearly 4 to 1 (50.0/11.6), indicating that it could be SO_4^{2-}, suggesting that the nanoparticles mainly consisted of $CuSO_4$ and Bi oxides. Position 2 (Figure 5f) had a lighter contrast and a complex composition, with ore-forming elements such as Cu and Mo (Table 2). In the SAED pattern, the diffraction spots were cluttered, indicating a variety of crystalline properties. Additionally, Cu and Mo were likely to exist as oxides.

4.2. Nanoparticles in Ascending Gas Flow

Natural Fe-bearing nanoparticles commonly appear in the ascending gas flow. A natural Fe-, Mn- and Cr-bearing nanoparticle with a small amount of Mn and Cr (ID8) (Table 2) is shown in Figure 6a. An interplanar d-spacing of 2.08 Å (10d = 2.08 nm) is measured in the HRTEM image. Interplanar d-spacings of 2.21 and 1.26 Å are calculated from the SAED pattern. These interplanar d-spacings are similar to those of the (202), (113), (220) lattice plane of Fe_2O_3 (PDF#33-0664) standard PDF card, suggesting that this nanoparticle contains Fe_2O_3.

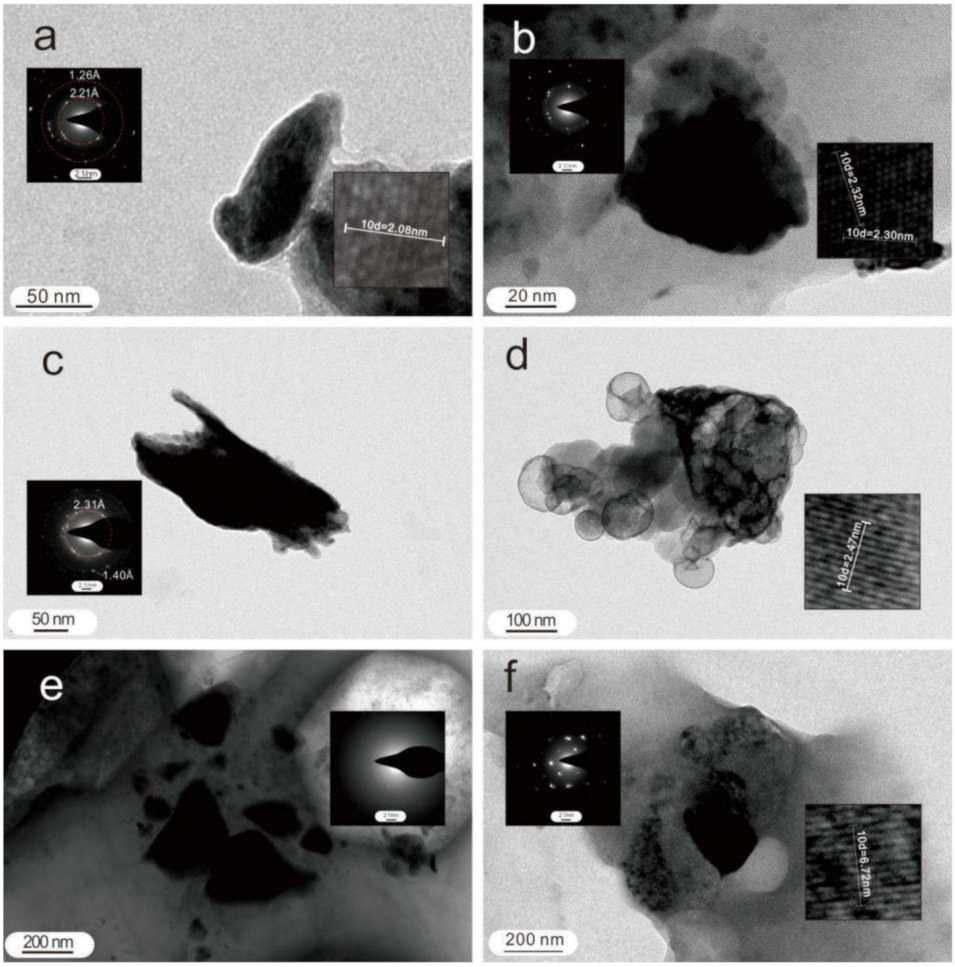

Figure 6. TEM photomicrographs of particles or aggregations carried by the ascending gas flow. (**a**) TEM image, SAED pattern and HRTEM image of an Fe-, Mn- and Cr-bearing particle (ID8). (**b**) TEM image, SAED pattern and HRTEM image of a Cu- and Pt-bearing particle (ID9). (**c**) TEM image, SAED pattern of a Cu- and Sn-bearing particle (ID10). (**d**) TEM image and HRTEM image of a Pb- and Zn-bearing aggregation (ID11). (**e**) TEM image, SAED pattern of several of Fe-, Cu-, Zn- and Bi-bearing particles (ID12). (**f**) TEM image, SAED pattern and HRTEM image of Mo- and Zn-bearing aggregation (ID13).

Large numbers of natural Cu-bearing nanoparticles are observed in ascending gas flow samples. Additionally, Cu-bearing nanoparticles usually exist in the form of CuO with a small amount of Pt or Sn. Figure 6b shows a Cu- and Pt-bearing nanoparticle (ID9). The primary components of the nanoparticle are O, Cu and Pt (Table 2). The SAED pattern indicates that this nanoparticle is polycrystalline, with many distributed diffraction spots. According to the HRTEM image (Figure 6b), the interplanar d-spacings of 10d = 0.230 and 0.232 nm (Figure 6b) are similar to those of the (111) lattice plane of the CuO (PDF#80-0076) standard PDF card. The atomic ratio of Cu to O in this nanoparticle is close to 1(40.71/55.16,

Table 2), suggesting that it is mainly a CuO nanoparticle. Figure 6c shows a natural Cu- and Sn-bearing nanoparticle (ID10) with a size of 100 × 200 nm^2. The nanoparticle has an irregular shape and contains O, Cu and Sn (Table 2). There are many diffraction spots irregularly distributed in the SAED pattern, suggesting that this nanoparticle is polycrystalline; thus, the nanoparticle may contain CuO and Sn oxides.

A natural aggregation consisting of several Pb- and Zn-bearing spherical nanoparticles (ID11) is shown in Figure 6d. The diameters of these nanoparticles ranged from 50 to 150 nm. One of the interplanar d-spacings measured 2.47 Å (10d = 2.47 nm), which matches the (200) lattice plane of ZnO_2 (PDF#13-0311). This aggregation is speculated to consist of Zn and Pb oxides.

In addition, Bi, V and Mo are detected in a few natural nanoparticles. For instance, several irregularly shaped Fe-, Cu-, Zn- and Bi-bearing nanoparticles (ID12, Table 2) with sizes ranging from 50 to 250 nm are shown in Figure 6e, and a Mo- and Zn-bearing nanoparticle (ID13, Table 2) is shown in Figure 6f.

4.3. Nanoparticles in Soil

A natural Au-Ag-bearing aggregation with a size of 250 × 300 nm^2 is shown in Figure 7a. The aggregation consists of several irregularly contrasted nanoparticles, with lighter contrast and bigger sizes. Numerous diffraction spots and clear lattice fringes are shown in the SEAD pattern (Figure 7b) and HRTEM image (Figure 7b), suggesting that this aggregation is mainly polycrystalline. Combined with EDS analysis (Figure 7d, Table 3), the nanoparticles are likely to be native gold, silver and Cu oxides.

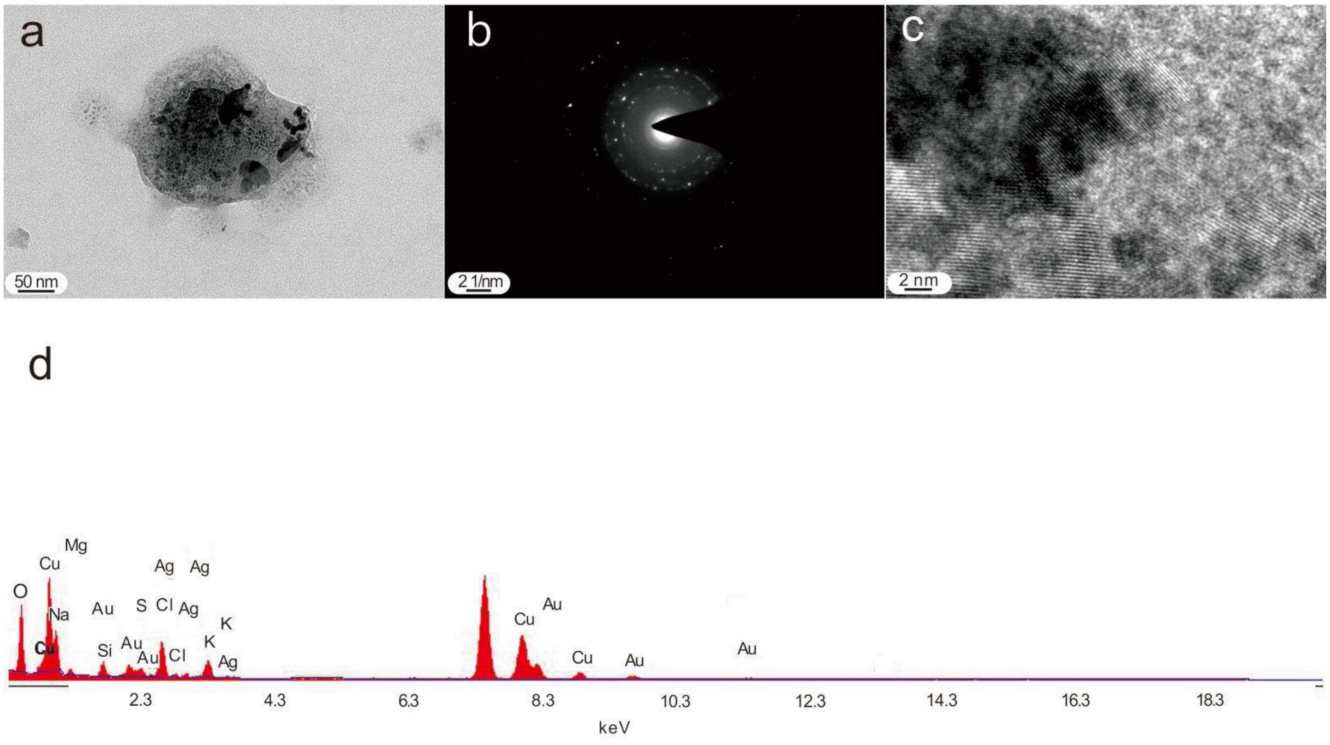

Figure 7. TEM photomicrographs of Au-bearng in the soil. (**a**) TEM image, SAED pattern (**b**), HRTEM image (**c**) and energy spectrum (**d**).

Figure 8a shows a natural irregularly shaped Fe-, Mn- and Cu-bearing nanoparticle (ID15), which consists of O, Fe, Si, Cr, Mn and small amount of Cu (Table 3). One of the interplanar d-spacings is 3.35 Å (10d = 3.35 nm). The SAED pattern indicates that the nanoparticle is polycrystalline with regularly distributed diffraction rings. Thus, this nanoparticle may be an Fe, Mn or Cr oxide. A natural Cu-bearing aggregation with high contrast (ID16) is formed by two nanoparticles, as shown in Figure 8b. The EDS result

(Table 3) shows that the aggregation mainly contains O, Cu and a small amount of S. Figure 8c shows a natural Cu- and Sn-bearing aggregation (ID17) with irregular shape. According to the SAED pattern, with many diffraction spots, the aggregation is composed of polycrystalline grains. The aggregation (Table 3) predominantly contains O, Cu and Sn, indicating that it mainly consists of oxides of Cu and Sn.

Table 3. The EDS data of particles and particle aggregations in soil (ID14-20) and shallow (ID21-24) and deep (ID25-28) groundwater.

Particle ID	Elements (%)	Au	Ag	O	Na	Mg	Al	Si	S	Cl	Ar	K	Ca	V	Cr	Mn	Fe	Co	Cu	Zn	As	Mo	Sn	Pb	Size/nm^2
14	wt%	3.9	2.1	30.4	11.6	1.8		2.2	1.1	4.6		2.3							39.9						250 × 300
	at%	0.6	0.6	55.1	14.6	2.2		2.3	1.0	3.7		1.7							18.2						
15	wt%			62.8				9.5							4.6	3.9	18.5		0.8						100 × 350
	at%			82.4				7.1							1.8	1.5	6.9		0.3						
16	wt%			47.1				3.5	5.7										43.7						200 × 400
	at%			74.8				3.2	4.5										17.5						
17	wt%			61.4				9.9											17.6				11.2		200 × 230
	at%			84.4				7.7											6.1				2.1		
18	wt%			52.2																47.8					100 × 150
	at%			81.7																18.3					
19	wt%			78.2	8.8			3.6		4.1		4.9								0.2				0.2	200 × 210
	at%			86.6	6.8			2.3		2.1		2.2								0.1				0.1	
20	wt%			51.6	30.4	8.8		2.3		3.6		2.5							0.7	0.1					290 × 300
	at%			62.4	25.6	7.0		1.6		2.0		1.3							0.2	0.1					
21	wt%			59.5	0.2		8.2	5.6				1.5	8.8			1.0	13.3			0.7	1.2				300 × 300
	at%			77.9	0.2		6.3	4.5				0.8	4.5			0.4	5.0			0.2	0.3				
22	wt%			12.6		0.6			0.5	0.3	0.2		1.1			0.3	1.0		76.8				6.5		80 × 80
	at%			36.5		1.2			0.8	0.4	0.3		1.3			0.3	0.8		56.0				2.5		
23	wt%			13.1				0.2	0.3			0.8			14.4	2.3	58.6		8.2			2.0			150 × 250
	at%			34.5				0.4	0.4			0.9			11.6	1.8	44.2		5.4			0.9			
24	wt%			31.5		0.8	0.8	0.8					1.1			1.3	56.9	6.7							100 × 200
	at%			60.7		1.0	0.9	0.9					0.8			0.8	31.4	3.5							
25	wt%			9.3	19.4									1.4			14.5	14.2		41.3					100 × 100
	at%			22.5	32.6									1.0			10.0	9.3		24.5					
26	wt%			9.8						0.2		2.4	1.0			1.0	1.8		34.1	3.5		46.2			200 × 300
	at%			33.5						0.4		3.4	1.4			1.0	1.8		29.4	3.0		26.4			
27	wt%			18.9									3.5				21.1		9.7				46.8		100 × 300
	at%			53.8									3.9				17.3		7.0				18.0		
28	wt%			15.4		0.6	0.3	0.3	12.8				0.3				68.7							1.6	180 × 250
	at%			36.3		0.9	0.5	0.4	15.0				0.3				46.3							0.3	

Many natural Zn- and Pb-bearing nanoparticles were observed in soil samples. Figure 8d shows a natural Zn-bearing nanoparticle (ID18) with an incomplete hexagon shape and a size of 100 × 150 nm^2. The EDS results (Table 3) show that it mainly consists of O and Zn, suggesting that it may be a ZnO nanoparticle. Pb and Zn are usually observed in the same natural nanoparticle or aggregation, and Figure 8e shows a natural Pb- and Zn-bearing aggregation (ID19). It only contains a small amount of Pb and Zn, indicating that these elements exist as a small thimbleful of impurities in the aggregation (Table 3). Mo and Bi were observed in a few natural nanoparticles. Figure 8f shows a natural aggregation (ID20) containing Bi and Mo. The EDS results (Table 3) show that it contains O, Na and a small amount of Cu, Zn, Mo and Bi, suggesting that the nanoparticles mainly consist of carbonates such as Na_2CO_3. Cu, Zn, Mo and Bi exist as a small thimbleful of impurities in the aggregation.

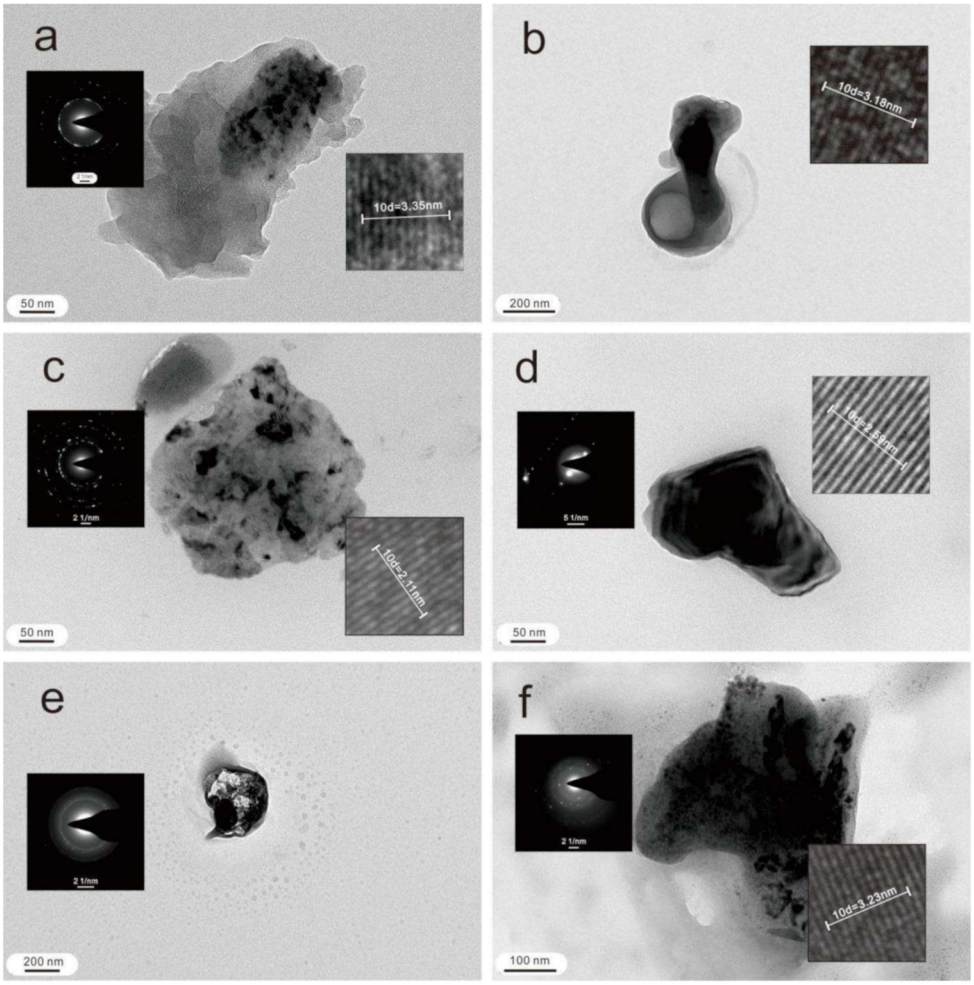

Figure 8. TEM photomicrographs of particles or aggregations in the soil. (**a**) TEM image, SAED pattern and HRTEM image of an Fe-, Mn- and Cu-bearing particle (ID14). (**b**) TEM image and HRTEM image of a Cu-bearing aggregation (ID15). (**c**) TEM image, SAED pattern and HRTEM image of a Cu- and Sn-bearing particle (ID16). (**d**) TEM image, SAED pattern and HRTEM image of a Zn-bearing particle (ID17). (**e**) TEM image and SAED pattern of a Pb- and Zn-bearing particle (ID18). (**f**) TEM image, SAED pattern and HRTEM image of a Cu-, Zn-, Bi- and Mo-bearing particle (ID19).

4.4. Nanoparticles in Groundwater

4.4.1. Nanoparticles in Shallow Groundwater

Figure 9a shows a natural Fe-, Zn- and As-bearing aggregation (ID21) with a size of 300 × 300 nm^2. It contains O, Al, Si, Ca, Fe and a small amount of Na, K, Zn and As (Table 3). The SAED pattern shows that it is polycrystalline, suggesting that this aggregation may consist of silicate crystals and a small amount of Fe, Zn and As oxides. Figure 9b shows a natural Cu- and Sn-bearing nanoparticle (ID22) that mainly consists of Cu and Sn oxides. The SAED pattern shows that it is polycrystalline with several diffraction spots.

Figure 9c shows a natural aggregation (ID23) with a complex composition. In the HRTEM image, crystalline interplanar d-spacings are clearly shown. It contains O, Fe, Cr, Mn, Cu and minor amounts of Mn, Mo, Si, S and K (Table 3), suggesting that it mainly contains Mn and Mo oxides. An Fe- and Co-bearing nanoparticle (ID24) of 200 × 100 nm^2 in size can be seen. It contains O, Fe and a small amount of Co, Mn, Mg, Al, Si and Ca (Table 3). The SAED pattern shows that it is polycrystalline with several irregular diffraction spots. Based on the element composition of the nanoparticle, it mainly consists of Fe oxides.

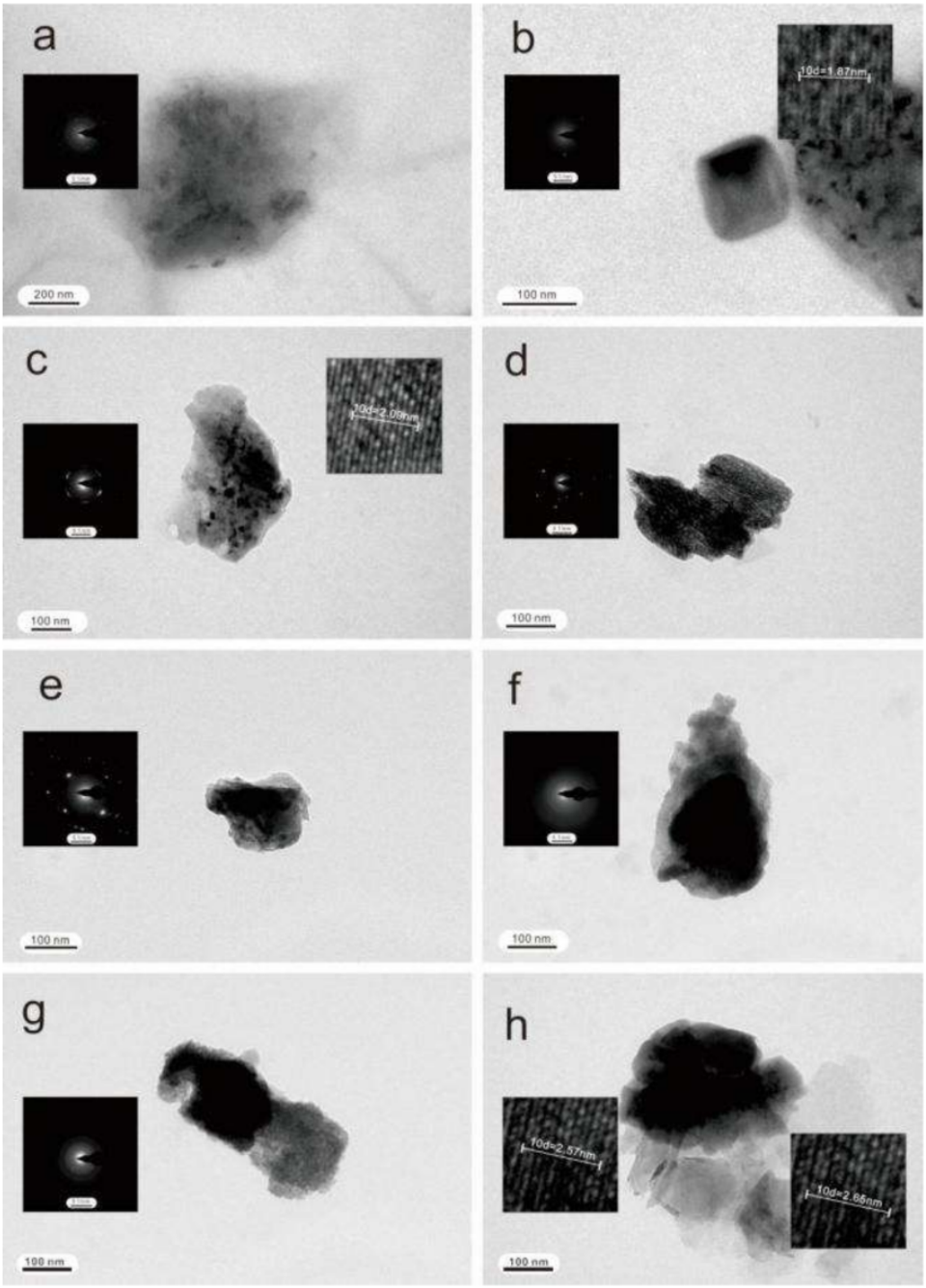

Figure 9. TEM photomicrograph of particles or aggregations in the well water (**a**–**d**) and in the deep groundwater (**e**–**h**). (**a**) TEM image and SAED pattern of an Fe-, Zn- and As-bearing aggregation (ID20). (**b**) TEM image, SAED pattern and HRTEM image of a Cu- and Sn-bearing particle (ID21). (**c**) TEM image, SAED pattern and HRTEM image of an Fe-, Cr-, Mn-, Cu-, Mo-bearing aggregation (ID21). (**d**) TEM image and SAED pattern of an Fe- and Co-bearing particle (ID23). (**e**) TEM image and SAED pattern of a V, Fe, Co and Zn-bearing particle (ID24). (**f**) TEM image and SAED pattern image of a Cu-, Mo- and Zn-bearing particle (ID25). (**g**) TEM image and SAED pattern of a Cu-, Sn- and Fe-bearing particle (ID26). (**h**) TEM image and HRTEM images of an Fe- and Pb-bearing aggregation (ID27).

4.4.2. Nanoparticles in Deep Groundwater

The natural nanoparticles in deep groundwater mainly contain the metal elements Fe, Cu, Zn, Pb, Sn, As, Co and V (Table 3; ID25-28). Figure 9e shows a natural V-, Fe-, Co- and Zn-bearing nanoparticle (ID25) with a size of 100 × 100 nm^2. It contains O (9.3%), Na (19.4%), V (1.4%), Fe (14.5%), Co (14.2%) and Zn (41.3%) (Table 3). There are some irregular diffraction spots in the SAED pattern, with polycrystalline features. Based on the element compositions, it may consist of Fe, Co and Zn oxides, as well as sodium carbonate and/or sodium bicarbonate. A natural Cu-, Mo- and Zn-bearing nanoparticle (ID26) is shown in Figure 9f. The nanoparticle contains O (9.8%), Cu (34.1%), Zn (3.5%), Mo (46.1%) and a small amount of K, Cl, Ca, Mn and Fe (Table 3). The SAED pattern shows it is amorphous without any diffraction spots, and it is likely to mainly consist of Cu, Mo and Zn oxides.

Figure 9g shows a natural Cu-, Sn- and Fe-bearing nanoparticle (ID27) with a size of 100×300 nm^2. It contains of O, Fe, Cu and Sn (Table 3). Polycrystalline features are shown in the SAED pattern, with some diffraction spots. Based on the above analysis, this nanoparticle likely consists of Fe, Cu and Sn oxides. A natural Fe- and Pb-bearing aggregation (ID28) is shown in Figure 9h. It has a complex composition and contains O, S, Fe and minor amounts of Pb, Mg, Al, and Si (Table 3). According to the EDS results, the atomic ratio of S to O was nearly 4 to 1 (15.0/36.3), indicating that it could be SO_4^{2-}. Two of the crystalline interplanar d-spacings are 0.265 and 0.257 nm (d-spacing data d (Å) = 2.65 and 2.57 Å), similar to the (221), (018) lattice plane d-spacings of the iron sulfate $Fe_2(SO_4)_3$ (PDF#42-0229) standard PDF card, suggesting that it may be a $Fe_2(SO_4)_3$ nanoparticle.

4.5. Nanoparticles in Background Area

In background ascending gas flow and soil samples, natural nanoparticles contain O, Na, Mg, Al, Si, S, K, Ca and Fe (Table 4; IDB1-B8). The ascending gas flow samples are mainly composed of natural nanoparticles containing Mg, K and Al (IDB1-B3), and the soil natural nanoparticles are mainly composed of Fe, Mg, Si, Al, Ca and K. They usually have an irregular shape and crystalline features, and their contrast is relatively uniform (Figure 10).

Table 4. The EDS data of particles and aggregations in background samples (IDB1-B3,ascending gas flow, IDB4-8, soil).

Particle ID	Elements (%)	O	Mg	Al	Si	S	K	Ca	Fe	Size/nm^2
B1	wt%	59.3	19.4		21.4					4000 × 6000
	at%	70.4	15.4		14.5					
B2	wt%	74.0	2.3	8.5	13.3		0.4	1.6	0.1	300 × 500
	at%	83.2	1.7	5.7	8.5		0.2	0.7	0.1	
B3	wt%	91.2			1.9			6.9		400 × 700
	at%	96.0			1.2			2.9		
B4	wt%	64.4	2.0	11.1	20.9		0.7	0.5	0.4	600 × 900
	at%	76.0	1.5	7.8	14.0		0.4	0.2	0.1	
B5	wt%	78.7	0.7	1.0	2.5			16.0	1.1	150 × 200
	at%	89.5	0.6	0.7	1.7			7.2	0.4	
B6	wt%	87.2			7.6	3.7			1.6	100 × 150
	at%	93.0			4.6	2.0			0.5	
B7	wt%	67.5		3.1	4.6			3.5	21.2	400 × 500
	at%	84.9		2.3	3.3			1.8	7.7	
B8	wt%	91.7						8.3		500 × 900
	at%	96.5						3.5		

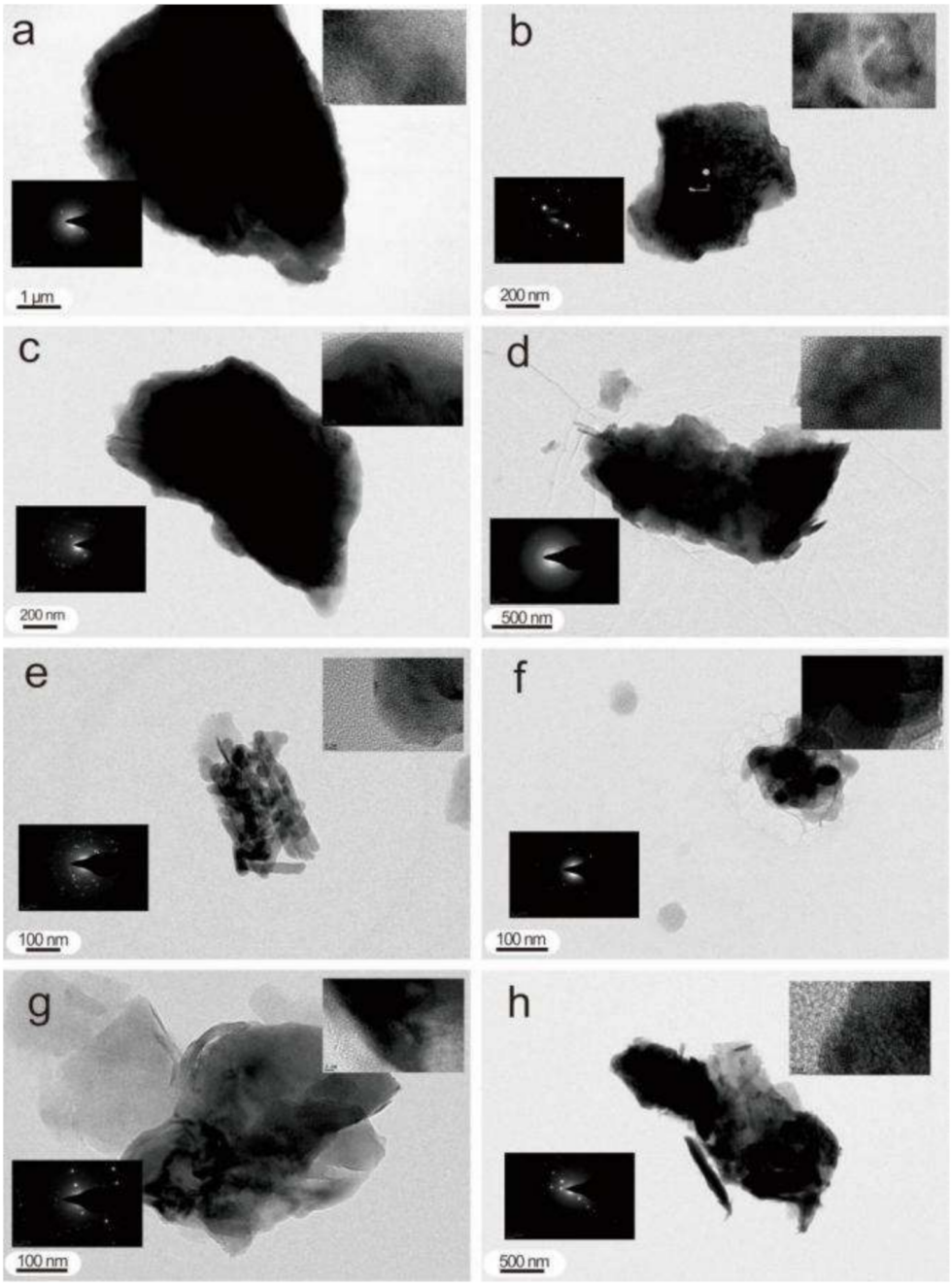

Figure 10. TEM photomicrograph of particles or aggregations in the (**a**–**c**) ascending gas flow and (**d**–**h**) in the soil. (**a**) TEM image, SAED pattern and HRTEM image of an Mg-, Si-bearing aggregation (IDB1). (**b**) TEM image, SAED pattern and HRTEM image of a Mg-, Al-, Si, Ca-, Fe-bearing particle (IDB2). (**c**) TEM image, SAED pattern and HRTEM image of a Si-, Ca-bearing aggregation (IDB3). (**d**) TEM image, SAED pattern and HRTEM image of a Mg-, Al-, Si-, K-, Ca-, Fe-bearing particle (IDB4). (**e**) TEM image, SAED pattern and HRTEM image of a Mg-, Al-, Si-, Ca-, Fe-bearing particle (IDB5). (**f**) TEM image, SAED pattern and HRTEM image of a Si-, Fe-bearing particle (IDB6). (**g**) TEM image, SAED pattern and HRTEM image of a Ca-bearing particle (IDB7). (**h**) TEM image SAED pattern and HRTEM images of an Fe- and Pb-bearing aggregation (IDB8).

5. Discussion

5.1. Summary of Nanoparticle Characteristics in Different Types of Sample

In this study, five types of samples in the Chaihulanzi gold deposit, China, were collected for comparative study, as well as ascending gas flow and soil in the background area. Based on TEM observations of natural nanoparticles in different types of samples, their characteristics were obtained, including their category, size, shape, lattice parameters, chemical component and association.

5.1.1. Nanoparticles in Deep-Seated Fault Gouges

The fault gouge samples were collected from multiple faults crosscutting the orebodies′ veins. In Chaihulanzi deposit, three stages of mineralization are defined: (I) K-feldspar-quartz-epidote (zircon U-Pb age: 256.6 ± 6.5 Ma [60]), (II) quartz-sericite-pyrrhotite (263.67 ± 0.99 Ma in this study), and (III) quartz-carbonate (LA-ICP-MS zircon U-Pb age: 132–138 Ma [61]). Gold mineralization occurs mainly in stages II and III, whose dominant ore minerals are native gold and Au-tellurite [56]. The ore-forming elements of natural nanoparticles in deep-seated fault gouge samples include Au, Fe, Cu, Zn, Pb, Sn, Bi, Mo and As (Table 2, ID1-7). In particular, the discovery of natural-Au-bearing nanoparticles (ID1) is a direct manifestation of the presence of ore-forming elements in the nanoparticles [54,56,57]. The element associations included Au-Cu, Fe-Pb-As-Mn, Fe-Cu-Mg, Zn-Fe-Co, Pb-Zn-Fe-Cu-Sn, Cu-Bi-Fe and Cu-Fe-Mo (Table 2). Natural nanoparticles in fault gouges ranged from 20 to 300 nm, and they exhibited different morphologies, including irregular shapes and regular hexagons (Figure 5). Some nanoparticles with clearly and sharp edges were observed (Figure 5c and d), as well as the distortion and dislocation of crystal lattices in the HRTEM images (Figure 5b), indicating that crystal lattices were subjected to stress [37,42,62], such as faulting [38].

5.1.2. Nanoparticles in Ascending Gas Flow and in Soil

The types and characteristics of natural metal-bearing nanoparticles in ascending gas flow and soil are highly similar (Tables 2 and 3, ID8-20). Both natural nanoparticles in the two types of samples included the metal elements Fe, Cu, Zn, Pb, Bi and Mo, which commonly exist in the form of oxides. The element associations of nanoparticles in the two types of samples both include Fe-Mn-Cr, Cu-Sn, Cu-Zn-Bi and Pb-Zn. Natural-Au-Ag-bearing nanoparticles were detected in soil samples (ID14). There were no natural-metal-bearing nanoparticles (except Fe) in the background area with the same overburden (Table 4, IDB1-B8), indicating that the origin of the metal elements observed in the natural nanoparticles of ascending gas flow and soil samples in the ore area is not surface overburden.

5.1.3. Nanoparticles in Shallow and Deep Groundwater

The metal elements of nanoparticles in shallow and groundwater were basically the same, including Fe, Cu, Zn, Sn, Mo, Mn, Mg, Co, Al, K, Ca, Si, O and S (Table 3, ID21-28). Elements related to concealed orebodies such as Cu, Zn and Mo were detected in both samples. There was also consistency in terms of element associations, including Fe-Zn (shallow: ID21; deep: ID25, ID26), Fe-Cu (shallow: ID22, ID23; deep: ID26, ID27), Cu-Sn (shallow: ID22; deep: ID27) and Fe-Co (shallow: ID24; deep: ID25) (Table 3). Metal oxides are speculated to be their existent form, such as Fe oxides in shallow (ID21, ID23, ID24) and deep (ID25, ID27) groundwater, or Cu oxides in shallow (ID22, ID23) and deep (ID26, ID27) groundwater. Most of these natural nanoparticles have crystalline properties and a few are amorphous (ID26).

5.1.4. Summary of Nanoparticle Characteristics in Various Types of Sample

The characteristics of natural nanoparticles in five types of samples are summarized and shown in Table 5.

Table 5. Summary of the nanoparticles characteristics in the different sample types.

Sample Type	Characteristics of the Nanoparticles		
	Type	**Element Association**	**Sharp**
Fault gouge sample	Fe oxide; Pb_2O_3; As oxide; Cu_2O; ZnO; Bi oxide; $CuSO_4$; Mo oxide	Fe-Pb-As-Mn; Fe-Cu-Mn; Zn-Fe-Co; Pb-Zn-Fe-Cu-Sn; Cu-Bi-Fe; Cu-Fe-Mo	Irregular shape, hexagon; some of them with twisted crystal lattices, always with sharp and clearly edges
Ascending gas flow sample	Fe oxide; CuO; Pb oxide; Zn oxide; Mo oxide	Fe-Mn-Cr; Cu-Pt; Cu-Sn; Pb-Zn; Fe-Cu-Zn-Bi; Zn-Mo	Subcircular, trigonal, strip or unregular shape; always with smooth edges
Soil sample	Cu oxide; Fe oxide; $CuSO_4$; Sn oxide; ZnO; Pb oxide	Fe-Mn-Cr-Cu; Fe-Cu; Cu-SnPb-Zn; Cu-Zn-Mo-Bi	Irregular shape, spherical, hexagon; always in the form of aggregation
Well (shallow) water sample	Fe oxide; Zn oxide; As oxide; CuO; Cu-Sn alloy; Mo oxide	Fe-Zn-As; Cu-Sn; Fe-Mn-Cr-Cu-Mn; Fe-Mn-Co	Irregular shape, rhomboid, always with smooth edges
Deep groundwater sample	Fe oxide; Zn oxide; Cu oxide; Mo oxide; Sn oxide; $Fe_2(SO_4)_3$	Fe-Co-Zn-V; Cu-Mo-Zn; Fe-Cu-Sn; Fe-Pb	Irregular shape, some of them with sharp edges

The natural nanoparticles in various types of samples have high similarity in terms of metal element composition (ID1-28, in Tables 2 and 3). It is generally observed that the samples contain Fe, Cu, Zn, Pb and Sn. Meanwhile, Au, Ag, Mo, Bi and As can also be observed. In addition, Pt and V can also be detected in some of the natural nanoparticles. The metal elements of the five types of sample commonly exist in the form of oxides or sulfates.

The element associations in various types of sample have a certain regularity. For instance, Fe often combines with Mn, Cr and Co; Sn often combines with the Cu; and Pb and Zn are often observed in the same natural nanoparticle (or aggregation).

The size of most of the natural single metal-bearing nanoparticles was less than 300 nm. In terms of shape, there were many irregular nanoparticles and aggregations. In both the deep fault gouge samples and well water samples were found ZnO and Cu oxide nanoparticles of hexagonal shape (ID4 and 22; Figures 5c and 9b).

Above all, natural nanoparticles in five types of shallow (soil, ascending gas flow and well water samples) and deep samples (fault gouge and deep groundwater samples) exhibit many common characteristics in terms of chemical composition, element associations and morphology, indicating that they may have a common origin.

5.2. The Relationship between Shallow and Deep Media and the Orebodies

In addition to metal oxides, natural nanoparticles in deep groundwater also exist in the form of sodium bicarbonate (ID25), indicating that deep groundwater is less affected by oxygen than shallow groundwater. First, in this study, the oxygen proportion of natural nanoparticles is higher in the surface media than in the deep media. Here, homogeneous media, deep-seated fault gouges and soils, deep groundwater and shallow groundwater are compared. In this study, the average weight percent (wt%) and atomic percent (wt%) of O in natural nanoparticles from the deep-seated fault gouges are 25.52% and 51.82% (ID1-7, Table 2), but those in the soil are 58.88% and 78.71% (ID14-20, Table 3), respectively. The average wt% and at% of O in deep groundwater are 13.35%, and 36.52% (ID25-28), while those in shallow groundwater are 29.17% and 52.24% (ID21-24), respectively. This evidence suggests that elemental ratios changed during the migration of natural nanoparticles from deep to shallow media. Second, metal elements have a higher chemical valency in shallow media. There exists Pb_2O_3 (ID5) with +3 and $CuSO_4$ (ID6) with +2 chemical valency in natural nanoparticles from deep-seated fault gouges. However, the Pb-bearing particles (ID19) in soil have a high proportion of O, which could form Pb oxides, PbO_x. This X value may be higher due to the large proportion of O, and the chemical valency of Pb could be higher than +3. Similarly, Cu may also have a higher chemical valency alongside the

higher proportion of O in the natural Cu-bearing nanoparticles of soil samples (ID15-18). For example, Cu in ID17 occurs in copper oxide, and because of the high O content, it has a higher chemical value than +2. In addition, the nanostructures of most natural nanoparticles in the surface media are diverse, characterized by polycrystalline mixed forms, including amorphous and crystalline mictures and crystallized nanoparticles [34]. These phenomena indicate that the natural nanoparticles in the shallow media (shallow groundwater and soil) could have migrated from deep media (deep groundwater and deep-seated fault gouges).

Based on the above analysis of particle characteristics in various media, we found that such characteristics are associated with concealed orebodies. The predominant metallic minerals of the Chaihulanzi deposit are gold, pyrite, chalcopyrite and sphalerite, as well as the ore-forming metal elements Au, Ag, Fe, Cu, Pb, Zn, Sn, As and Mo [45–47,57]. First, ore-forming elements are represented in these particles, such as Au (ID1) and As (ID2, ID5) in deep fault gouges, Cu (ID9, ID10, ID12) and Zn (ID11-13) in ascending gas flows, Au (ID14) and Sn (ID17) in soil and Co (ID24, ID25) and Mo (ID23, ID26) in shallow groundwater samples. The Au-Cu element association in nanoparticles from deep-seated fault gouge (ID1) and soil (ID14) samples reflects the Au-bearing concealed orebodies [49]. The Fe-As element association (ID2, ID5, ID21) in natural nanoparticles may be the cause of arsenic (As) always being incorporated into pyrite as an impurity [62–64]. S is detected in natural Fe- and As-bearing particles (ID2, 3), and may be originally derived from pyrite. The element associations of these natural nanoparticles are consistent with those of major minerals in this deposit. Au-Cu (ID1) corresponds to native gold, Fe-Cu-Mg-S (ID6, ID7) to chalcopyrite, and Pb-Fe-As (ID5) to galena. The Pb-Zn association (ID5, ID11, ID19) is likely to be related to the paragenesis of galena and sphalerite in the deep orebodies. Natural Cu-Sn-bearing particles are observed in five types of samples (ID5, ID10, ID17, ID22, ID27), which are closely related to the fact that the Chaihulanzi Au deposit generally contains Sn [65]. The above evidence suggests that natural metal-bearing nanoparticles in various types of sample are closely related to concealed orebodies.

The ore-forming elements contained in natural nanoparticles can reflect the existence of orebodies. A Au-Co-Cr-bearing nanoparticle from concealed orebodies at depths of more than 1000 m from the surface can be used to identify gold concealed orebodies [35]. Zn-Cu-bearing nanoparticles in the surface media groundwater can be used as a representative source of information of concealed orebodies [32,34]. Studies have shown that human mining, smelting and utilization activities could produce a large number of Pb-bearing nanoparticles that are widely distributed in natural media [66–69]. No natural Pb-bearing nanoparticles were found in shallow groundwater samples, and only a few nanoparticles with low Pb content were observed in deep groundwater samples, indicating that the samples were not contaminated by human activities. Moreover, in the background ascending gas flow and soil samples, natural-metal-bearing nanoparticles were hardly detected, which was related to mineralization (Table 4). In addition, there was no pollution from domestic or industrial sources. Therefore, these natural ore-bearing nanoparticles originate from concealed orebodies.

5.3. Formation of Ore-Bearing Nanoparticles

Multiple geological processes could influence the formation of nanoparticles [62]. Previous studies on the nanogeoscience of deposits indicated that nanoparticles can be formed by the processes of mineralization, such as magmatic action and the hydrothermal process [25,70,71]. In deposits, the formation of nanoparticles is closely related to the enrichment of metallogenic elements [72,73]. Gold nanoparticles can be formed by the direct precipitation of hydrothermal fluid or exsolved from other substances in the later stages of evolution of the deposit [71].

In this study, a large number of natural ore-bearing nanoparticles in the form of oxides and sulfates were observed, which are likely to be the products of the oxidation of the metal sulfide in the orebodies. Additionally, the S^{6+} in SO_4^{2-} of sulfates is transformed from the

S^{2-} in the sulfide minerals of the orebodies by oxidation [26,28]. $CuSO_4$ (ID6) in deep fault gouge samples and $Fe_2(SO_4)$ (ID28) in deep groundwater samples were the products of the oxidation of sulfide minerals in this deposit. On the other hand, in the fault gouge samples, the distortion and dislocation of crystal lattices were observed (Figure 5b). This phenomenon may be related to the mechanical fracture of natural nanoparticles caused by fault activity. In addition, there are many faults and fissures in the deposit [46,47,49,50,56,57], which provides the prerequisite for the formation of nanoparticles by faulting [32–36] and acts as a good conduit for oxygen by oxidation [74]. Thus, these natural nanoparticles were formed during the faulting and oxidation.

5.4. Migration Mechanism of the Ore-Bearing Nanoparticles

Based on the above analysis, natural ore-bearing nanoparticles are produced from concealed orebodies during faulting and oxidation. These nanoparticles are highly susceptible to migration due to their particular size [30,40,75]. Due to the temperature and pressure gradient [76,77], the ascending gas flows from the Earth's interior can carry these ore-bearing nanoparticles upward [78–81]. On the other hand, ore-bearing nanoparticles can also reach the surface by groundwater flow transportation [75,82] due to topography or the pressure between the aquifers [74,83]. Natural ore-bearing nanoparticles are carried by deep groundwater and migrate to shallow groundwater (such as well water, referred to in this study), during which element proportion, metal chemical valence, and nanostructure change, as described above. The entire migration pattern is shown in Figure 11.

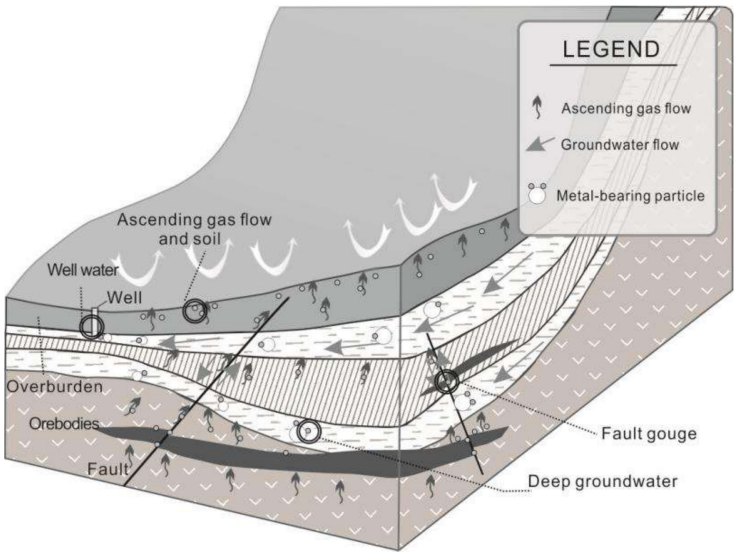

Figure 11. Schematic diagram: migration of ore-bearing particles in the Chaihulanzi deposit.

Nanoparticles are generally charged, with a high surface-to-volume ratio [84]. Thus, they have excellent absorptivity [40,58]. Recent research showed that the ore-bearing nanoparticles are absorbed and migrated by other nanoparticles [31,33,35,85]. The sorption of gold nanoparticles by sulfide via electrostatic interaction was confirmed by a synthesis experiment [86]. In this study, many natural ore-bearing nanoparticles were absorbed by other natural nanoparticles in deep-seated fault gouge (Figure 5e,f; ID6 and 7), ascending gas flow (Figure 6f; ID13), soil (Figure 8b; ID15), and groundwater samples (Figure 8a; ID20) indicating that the phenomenon of natural ore-bearing nanoparticles being absorbed and aided in migration by other natural nanoparticles is universal. In short, the natural ore-bearing nanoparticles are produced from concealed orebodies during faulting and oxidation, and are carried and transported by groundwater and ascending gas flows to the surface, during which some nanoparticles are absorbed by other particles.

5.5. The Significance of Ore-Bearing Nanoparticles in Different Media for Prospecting

In this study, the species and morphology of the natural ore-bearing nanoparticles are similar in the deep (deep-seated fault gouge and deep groundwater) and surface media (ascending gas flow, soil and well water) (Table 5), which provides confirmation of the consistency of the origin of natural ore-bearing nanoparticles. As discussed above, natural ore-bearing nanoparticles can be carried and aided in migration to the surface by groundwater and ascending gas flow, and some are present in fault gouges and soil. Ore-bearing elements can be brought to the surface in the form of nanoparticles. Therefore, these natural ore-bearing nanoparticles in the surface media could be used for exploration.

Natural single nanoparticles in surface media, containing information about concealed orebodies, are collected and analyzed for prospecting purposes. Compared with the traditional geochemistry prospecting method relying on element content, the use of natural nanoparticles can provide more guiding parameters, including nanoparticle morphology, lattice parameters, chemical components and association. Moreover, the prospecting information obtained from natural nanoparticle characteristics is more intuitive compared with that obtained by geophysical exploration, and could directly reflect the information of deep concealed orebodies, including their extent, elements, main mineral association, deposit types, etc.

6. Conclusions

From the TEM analysis of natural single nanoparticles in various media, including deep-seated fault gouges, ascending gas flows, soil, shallow groundwater and deep groundwater, the characteristics of these natural nanoparticles (and/or aggregations), including their category, size, shape, chemical components and association, are obtained. Based on the analyses above, we discussed the relationship between deep and shallow media, and the formation and migration mechanism of the natural ore-bearing nanoparticles, as well as their significance to prospecting. The following conclusions were reached:

I. The natural nanoparticles in the five types of samples generally contain ore-forming elements, including Au, Ag, Fe, Cu, Zn, Pb, Sn, As, Mo and Bi. Additionally, element associations such as Au-Cu, Fe-Cu, Pb-Zn, Cu-Sn and Fe-As are commonly observed in different types of samples. The sizes of the natural single ore-bearing nanoparticles are mostly below 300 nm. The shapes of the natural nanoparticles are varied, including spheres, hexagon, rhombuses and irregular shapes.

II. When the natural ore-bearing nanoparticles migrate from deep (deep groundwater and deep-seated fault gouge) to the surface media (shallow groundwater, soil and ascending gas flow), the proportion of O and the metal elements' chemical valence may become higher. The nanostructure is shown to take both mixed amorphous and crystalline and crystallized form. Excluding the influence of human activities, by comparing the background area and previous work, it can be inferred that these natural ore-bearing nanoparticles originate from concealed orebodies.

III. The ore-bearing metal elements mainly exist in the form of oxides and sulfates. The distortion and dislocation of crystal lattices in the fault gouge samples are observed. Additionally, the above evidence suggest that faulting and oxidation are the primary mechanisms of formation of natural ore-bearing nanoparticles.

IV. Natural nanoparticles are carried by groundwater and ascending gas flow and migrate to the surface due to temperature, pressure gradients, topography or the pressure between the aquifers.

V. Natural single ore-bearing nanoparticles migrate from the concealed orebodies into the surface media and are analyzed by TEM for prospecting purposes. The characteristics of these nanoparticles can directly reflect the information of the orebodies, including their extent, elements, main mineral association, and deposit types, which can then be used to guide prospecting.

Author Contributions: Writing original draft, Data analysis/evidence collection, M.L.; Conceptualization, Data curation, Supervision, Writing-Reviewing and editing, Funding acquisition, J.C.; Sample collection, Samples prepare, Performing the experiments, Z.W.; Visualization, Investigation, G.W. All authors have read and agreed to the published version of the manuscript.

Funding: This research was funded by National Natural Science Foundation of China (Grant Nos. 41873044, 41473040 and 41030425).

Data Availability Statement: The data presented in this work are available on request from the corresponding author.

Acknowledgments: The authors wish to thank Huang Qingli of the Instrument Analysis Centre at Yangzhou University for the assistance in TEM analysis and Chaihulanzi Mine Group. We also sincerely appreciate Editor Sutita Changsing and two anonymous reviewers for providing constructive suggestions.

Conflicts of Interest: The authors declare no conflict of interest.

References

1. Kristiansson, K.; Malmqvist, L. Evidence for nondiffusive transport of 86Rn in the ground and a new physical model for the transport. *Geophysics* **1982**, *47*, 1444–1452. [CrossRef]
2. Kristiansson, K.; Malmqvist, L. Trace elements in the geogas and their relation to bedrock composition. *Geoexploration* **1987**, *24*, 517–534. [CrossRef]
3. Tong, C.; Li, J. A new method searching for concealed mineral resources: Geogas prospecting based on nuclear analysis and accumulation sampling. *J. China Univ. Geosci.* **1999**, *10*, 329–332.
4. Khalil, M.; Jan, B.M.; Tong, C.W.; Berawi, M.A. Advanced nanomaterials in oil and gas industry: Design, application and challenges. *Appl. Energy* **2017**, *191*, 287–310. [CrossRef]
5. Arne, D.C.; Stott, J.E.; Waldron, H.M. Biogeochemistry of the Ballarat East Goldfield, Victoria, Australia. *J. Geochem. Explor.* **1999**, *67*, 1–14. [CrossRef]
6. Johanna, L.; Jorg, E.; Martin, Z. Geogas transport in fractured hard rock—Correlations with mining seismicity at 3.54 km depth, TauTona gold mine, South Africa. *Appl. Geochem.* **2011**, *26*, 2134–2146.
7. Wan, W.; Wang, M.; Hu, M.; Gao, Y. Identification of metal sources in Geogas from the Wangjiazhuang copper deposit, Shandong, China: Evidence from lead isotopes. *J. Geochem. Explor.* **2017**, *172*, 167–173. [CrossRef]
8. Clark, J.R.; Meier, A.L.; Riddle, G. Enzyme leaching of surficial geochemical samples for detecting hydromorphic trace-element anomalies associated with precious-metal mineralized bedrock buried beneath glacial overburden in northern Minnesota. In Proceedings of the Gold'90 Symposium-Gold'90, Salt Lake City, UT, USA, 26 February–1 March 1990; pp. 189–207.
9. Williams, T.M.; Gunn, A.G. Application of enzyme leach soil analysis for epithermal gold exploration in the Andes of Ecuador. *Appl. Geochem.* **2002**, *17*, 367–385. [CrossRef]
10. Ryss, Y.; Goldberg, I. The partial extraction of metals (CHIM) method inmineral exploration. *Method Tech. ONTI VITR Leningr.* **1973**, *84*, 5–19.
11. Antropova, L.V.; Goldberg, I.S.; Voroshilov, N.A.; Ryss, J.S. New methods of regional exploration for blind mineralization: Application in the USSR. *J. Geochem. Explor.* **1992**, *43*, 157–166. [CrossRef]
12. Luo, X.; Hou, B.; Wen, M.; Zeng, N.; John, K.; Roger, F.; Adrian, F. CHIM-geoelectrochemical method in search of concealed mineralisation in China and Australia. *Chin. J. Geochem.* **2008**, *27*, 198–202. [CrossRef]
13. Ke, D.; Zhang, W.; Li, L.; Wu, G.; Liu, H. Preliminary studies on deep-penetrating geochemical methods in exploration for concealed volcanic-type uranium deposit. *IOP Conf. Ser. Earth Environ. Sci.* **2020**, *569*, 012103. [CrossRef]
14. Mann, A.; Birrell, R.; Humphreys, D.; Perdrix, J. Application of the mobile metal ion technique to routine geochemical exploration. *J. Geochem. Explor.* **1998**, *61*, 87–102. [CrossRef]
15. Turner, N.; Mills, D.; Fedikow, M.; Prince, P. The evaluation of geological exploration samples using multi-element mobile metal ion (MMI-M) selective weak extraction and inductively coupled plasma mass spectrometry (ICP-MS). *Geochem. Case Hist. Geochem. Explor. Methods.* **2007**, *7*, 793–977.
16. Hu, Y.; Liu, X.; Luo, X.; Nakagoshi, N. Geoelectrochemical-extraction measurement method to look for hidden lead-zinc ore deposit and prospecting effect. *Adv. Mat. Res.* **2013**, *734*, 95–99. [CrossRef]
17. Xu, Z.; Liang, B.; Geng, Y.; Liu, T.; Wang, Q. Extraction of soils above concealed lithium deposits for rare metal exploration in Jiajika area: A pilot study. *Appl. Geochem.* **2019**, *107*, 142–151. [CrossRef]
18. Malmqvist, L.; Kristiansson, K. Experimental evidence for an ascending microflow of geogas in the ground. *Earth Planet. Sci. Lett.* **1984**, *70*, 407–416. [CrossRef]
19. Kristiansson, K.; Malmqvist, L.; Persson, W. Geogas prospecting: A new tool in the search for concealed mineralizations. *Endeavour* **1990**, *14*, 28–33. [CrossRef]
20. Gold, T.; Soter, S. The deep earth-gas hypothesis. *Sci. Am.* **1980**, *242*, 132–138. [CrossRef]
21. Morner, N.; Etiope, G. Carbon degassing from the lithosphere. *Glob. Planet. Change* **2002**, *33*, 185–203. [CrossRef]

22. Annunziatellis, A.; Ciotoli, G.; Lombardia, S.; Nolasco, F. Short- and long-term gas hazard: The release of toxic gases in the Alban Hills volcanic area (central Italy). *J. Geochem. Explor.* **2003**, *77*, 93–108. [CrossRef]
23. Bond, C.E.; Kremer, Y.; Johnson, G.; Hicks, N.; Lister, R.; Jones, D.J.; Haszeldine, S.; Saunders, I.; Gilfillan, S.M.V.; Shipton, Z.K.; et al. The physical characteristics of a CO2 seeping fault: The implications of fracture permeability for carbon capture and storage integrity. *Int. J. Greenh. Gas Control* **2017**, *61*, 49–60. [CrossRef]
24. Gilfillan, S.M.V.; Györe, D.; Flude, S.; Bond, C.E.; Hicks, N.; Lister, R.; Jones, D.G.; Kremer, R.S.H.; Stuart, F.M. Noble gases confirm plume-related mantle degassing beneath Southern Africa. *Nat. Commun.* **2019**, *10*, 5028. [CrossRef]
25. Tong, C.; Li, J.; Ge, L.; Yang, F. Experimental observation of the nano-scale particles in geogas matters and its geological significance. *China. Sci. China Ser. D* **1998**, *41*, 325–329.
26. Cao, J.; Hu, R.; Liang, Z.; Peng, Z. TEM observation of geogas-carried particles from the Changkeng concealed gold deposit, Guangdong Province, South China. *J. Geochem. Explor.* **2009**, *101*, 247–253. [CrossRef]
27. Cao, J.; Xiong, Z.; Liu, C. Method for Prospecting with Geo-Gas Particles. CN Patent Application 2010101544226, 14 April 2010.
28. Cao, J.; Lu, M.; Hu, G. Method for Predicting Concealed Deposits using Chemical Composition Data from Single Nanoparticles. CN Patent Application 2020101001628, 18 February 2020.
29. Li, Y.; Cao, J.; Hopke, P.; Holub, R.; Jiang, T. The discovery of the metallic particles of groundwater from the Dongshengmiao polymetallic deposit, Inner Mongolia, and their prospecting significance. *J. Geochem. Explor.* **2016**, *161*, 49–61. [CrossRef]
30. Cheng, S.; Cao, J.; Li, Y.; Hu, G.; Yi, Z. TEM observations of particles in groundwater and their prospecting significance in the Bofang copper deposit, Hunan, China. *Ore Geol. Rev.* **2018**, *95*, 382–400. [CrossRef]
31. Liu, X.; Cao, J.; Li, Y.; Hu, G.; Wang, G. A study of metal-bearing nanoparticles from the Kangjiawan Pb-Zn deposit and their prospecting significance. *Ore Geol. Rev.* **2019**, *105*, 375–386. [CrossRef]
32. Liu, X.; Cao, J.; Dang, W.; Lin, Z.; Qiu, J. Nanoparticles in groundwater of the Qujia deposit, eastern China: Prospecting significance for deep-seated ore resources. *Ore Geol. Rev.* **2020**, *120*, 103417. [CrossRef]
33. Yi, Z.; Cao, J.; Jiang, T.; Wang, Z. Characterization of metal-bearing particles in groundwater from the Weilasituo Zn-Cu-Ag deposit, Inner Mongolia, China: Implications for mineral exploration. *Ore Geol. Rev.* **2020**, *117*, 103270. [CrossRef]
34. Lu, M.; Cao, J.; Liu, X.; Qiu, J. Nanoparticles in various media on surfaces of ore deposits: Study of the more than 1000 m deep concealed Shaling gold deposit. *Ore Geol. Rev.* **2021**, *139*, 104466. [CrossRef]
35. Mi, Y.; Cao, J.; Wu, Z.; Wang, Z. Transmission Electron Microscopy Analysis on Fault Gouges from the Depths of the Bairendaba Polymetallic Deposit, Inner Mongolia, China. *J. Nanosci. Nanotechnol.* **2017**, *17*, 6549–6557. [CrossRef]
36. Wang, G.; Cao, J.; Dai, D. TEM analysis of nano-or near-nanoparticles in fault gouge from the Kaxiutata iron deposit (CHN) and the implications for ore body exploration. *J. Geochem. Explor.* **2019**, *207*, 106390. [CrossRef]
37. Cao, J. Characteristics, formation and migration of the particles carried by ascending gas flow from the concealed metal deposits. *Earth Sci. Front.* **2012**, *19*, 113–119, (In Chinese with English abstract).
38. Hu, G.; Cao, J.; Hopke, P.; Holub, F. Study of carbon-bearing particles in ascending geogas flows in the Dongshengmiao polymetallic pyrite deposit, inner Mongolia China. *Resour. Geol.* **2015**, *65*, 13–26. [CrossRef]
39. Wang, Z.; Cao, J.; Qiu, J.; Liu, X. Ore-forming elements and their distribution of nanoparticles in the updraft from the Sanshandao concealed deposit, China. *Ore Geol. Rev.* **2021**, *138*, 104371. [CrossRef]
40. Luo, S.; Cao, J.; Yan, H.; Yi, J. TEM observations of particles based on sampling in gas and soil at the Dongshengmiao polymetallic pyrite deposit, Inner Mongolia, Northern China. *J. Geochem. Explor.* **2015**, *158*, 95–111. [CrossRef]
41. Jiang, T.; Cao, J.; Wu, Z.; Wu, Y.; Zeng, J.; Wang, Z. A TEM study of particles carried by ascending gas flows from the Bairendaba lead-zinc deposit, Inner Mongolia, China. *Ore Geol. Rev.* **2019**, *105*, 18–27. [CrossRef]
42. Hu, G.; Cao, J.; Jiang, T.; Wang, Z.; Yi, Z. Prospecting Application of Nanoparticles and Nearly Nanoscale Particles Within Plant Tissues. *Resour. Geol.* **2017**, *67*, 316–329. [CrossRef]
43. Hu, G.; Cao, J.; Jiang, T. Discovery and prospecting significance of metal-bearing nanoparticles within natural invertebrate tissues. *Ore Geol. Rev.* **2018**, *99*, 151–165. [CrossRef]
44. Luo, X.; Cao, J. Discovery of nano-sized gold particles in natural plant tissues. *Environ. Chem. Lett.* **2018**, *16*, 1441–1448. [CrossRef]
45. She, H.; Xu, G.; Zhou, R. The tectonic and magmatic activities in early Mesozoic and their controlling on gold mineralization in Honghuagou gold field, Inner Mongolia. *China Geosci.* **2000**, *14*, 408–416, (In Chinese with English abstract).
46. She, H.; Wang, Y.; Li, Q.; Zhang, D.; Feng, C.; Li, D. The mafic granulite xenoliths and its implications to mineralization in chaihulanzi gold deposit, inner mongolian, China. *Acta Geol. Sini.* **2006**, *80*, 863–875, (In Chinese with English abstract).
47. Yang, Y.; She, H.; Xu, G.; Zheng, D.; Fu, D.; Cui, C. Yanshanian magmatic rocks and gold deposits of Chaihulanzi gold field, inner mongolia. *Acta Petrol. Sin.* **1999**, *15*, 475–483.
48. Yang, J.; Wu, F.; Wilde, S. A review of the geodynamic setting of large-scale Late Mesozoic gold mineralization in the North China craton: An association with lithospheric thinning. *Ore Geol. Rev.* **2003**, *23*, 125–152. [CrossRef]
49. Liu, H.; Liu, J.; Yu, C.; Ye, J.; Zeng, Q. Integrated geological and geophysical exploration for concealed ores beneath cover in the chaihulanzi goldfield, northern China. *Geophys. Prospect.* **2006**, *54*, 605–621. [CrossRef]
50. Zhang, Y.; Li, Y.; Zhang, Y. Methane-rich Fluid of Chaihulanzi Gold Deposit. *Acta Geol. Sini. (Engl. Ed.)* **2014**, *88*, 1214–1215. [CrossRef]
51. Zhang, Y.; Li, Y.; Li, F.; Zhang, H.; Chong, S. Characteristic and essence of rubefication in wall rock alteration of Anjiayingzi gold deposit in Harqin banner, Inner Mongolia. *Acta Petrol. Sin.* **2014**, *30*, 576–588.

52. Deng, J.; Wang, Q. Gold mineralization in China: Metallogenic provinces, deposit types and tectonic framework. *Gondwana Res.* **2016**, *36*, 219–274. [CrossRef]
53. Goldfarb, R.J.; Qiu, K.; Deng, J. Orogenic gold deposits of China. *Soc. Econ. Geol. Spec. Publ.* **2019**, *22*, 263–324.
54. Shi, K.; Wang, K.; Wang, R.; Ma, X.; Sun, L.; Yang, H. Geological, fluid inclusion, and O-C-S-Pb-He-Ar isotopic constraints on the genesis of the Honghuagou lode gold deposit, northern North China Craton. *Geochemistry* **2021**, *81*, 125807. [CrossRef]
55. Yuan, J.; Zhang, H.; Tong, Y.; Gao, J.; Xiao, R. Sources of metals and fluids for the Taijiying gold deposit on the northern margin of the North China Craton. *Ore Geol. Rev.* **2021**, *139*, 104593. [CrossRef]
56. Shi, K.; Wang, K.; Ulrich, T.; Ma, X.; Wang, W.; Wang, R. Early Permian lode gold mineralization in the northern North China Craton: Constraints from S-Pb isotope geochemistry and pyrite Re-Os geochronology of the Chaihulanzi deposit. *J. Asian Earth Sci.* **2021**, *218*, 104867. [CrossRef]
57. Qu, Y.; Xie, Y.; Yu, C.; Xia, J.; Xu, D.; Li, X. Geology, geochronology and tectonic setting of the Chaihulanzi gold deposit in Inner Mongolia, China. *Ore Geol. Rev.* **2021**, *134*, 104152. [CrossRef]
58. Wei, X.; Cao, J.; Holub, R.F.; Hopke, P.K.; Zhao, S.J. TEM study of geogas-transported nanoparticles from the Fankou lead-zinc deposit, Guangdong Province, South China. *J. Geochem. Explor.* **2013**, *128*, 124–135. [CrossRef]
59. Wang, Z.; Cao, J.; Lin, Z.; Wu, Z. Characteristics of soil particles in the Xiaohulishan deposit, Inner Mongolia, China. *J. Geochem. Explor.* **2016**, *169*, 30–42. [CrossRef]
60. Shao, J.; Zhang, Z.; She, H.; Liu, D. The discovery of Phanerozoic granulite in Chifeng area of North Craton and its implication. *Earth Sci. Front.* **2012**, *19*, 188–198, (In Chinese with English abstract).
61. Yang, Y.; Gao, F.; Chen, J.; Zhou, Y.; Zhang, J.; Jin, X.; Zhang, Y. Zircon U-Pb ages of mesozoic volcanic rocks in Chifeng. *Area J. Jilin Univ. Earth Sci. Ed.* **2012**, *42*, 257–267, (In Chinese with English abstract).
62. Cline, J.S. Timing of gold and arsenic sulfide mineral deposition at the Getchell Carlin-type gold deposit, North-Central Nevada. *Econ. Geol.* **2001**, *96*, 75–89. [CrossRef]
63. Morey, A.; Tomkins, A.; Bierlin, F.; Wienberg, R.; Davidson, G. Bimodal distribution of gold in pyrite and arsenopyrite: Examples from the Archean Boorara and Bardoc shear systems, Yilgarn craton, Western Australia. *Econ. Geol.* **2008**, *103*, 599–614. [CrossRef]
64. Deditius, A.P.; Utsunomiya, S.; Reich, M.; Kesler, S.E.; Ewing, R.C.; Hough, R.; Walshe, J. Trace metal nanoparticles in pyrite. *Ore Geol. Rev.* **2011**, *42*, 32–46. [CrossRef]
65. Qin, K.; Cao, M.; Hollings, P.; Watanabe, Y. The metallogenic system deep structure and formation process for the northeastern china compound orogenic belt: Introduction. *Ore Geol. Rev.* **2022**, *146*, 104960. [CrossRef]
66. Shotyk, W.; Weiss, D.; Kramers, J.D.; Frei, R.; Cheburkin, A.K.; Gloor, M.S. Geochemistry of the peat bog at Etang de la Gruère, Jura Mountains, Switzerland, and its record of atmospheric Pb and lithogenic trace metals (Sc, Ti, Y, Zr, and REE) since 12,370 14C yr BP. *Geochim. Cosmochim. Acta.* **2001**, *65*, 2337–2360. [CrossRef]
67. Schindler, M.; Santosh, M.; Dotto, G.; Silva, L.F.O.; Hochella, M.F. A review on Pb-bearing nanoparticles, particulate matter and colloids released from mining and smelting activities. *Gondwana Res.* **2022**, *110*, 330–346. [CrossRef]
68. Schindler, M.; Kamber, B.S. High-resolution lake sediment reconstruction of industrial impact in a world-class mining and smelting center, Sudbury, Ontario, Canada. *Appl. Geochem.* **2013**, *37*, 102–116. [CrossRef]
69. McConnell, J.R.; Wilson, A.I.; Stohl, A.; Steffensen, J.P. Lead pollution recorded in Greenland ice indicates European emissions tracked plagues, wars, and imperial expansion during antiquity. *Proc. Natl. Acad. Sci. USA* **2018**, *115*, 5726–5731. [CrossRef]
70. Palenik, C.; Utsunomiya, S.; Reich, M.; Kesler, S.; Wang, L.; Ewing, R. "Invisible" gold revealed: Direct imaging of gold nanoparticles in a Carlin-type deposit. *Am. Mineral.* **2004**, *89*, 1359–1366. [CrossRef]
71. Hastie, E.C.G.; Kontak, D.J.; Lafrance, B. Gold remobilization: Insights from gold deposits in the Archean Swayze greenstone belt, Abitibi Subprovince, Canada. *Econ. Geol.* **2020**, *115*, 241–277. [CrossRef]
72. Zhou, H.; Sun, X.; Cook, N.; Lin, H.; Fu, Y.; Zhong, R.; Brugger, J. Nano- to micron-scale particulate gold hosted by magnetite: A product of gold scavenging by bismuth melts. *Econ. Geol.* **2017**, *112*, 993–1010. [CrossRef]
73. Hough, R.M.; Noble, R.R.P.; Hitchen, G.J.; Hart, R.; Reddy, S.M.; Saunders, M.; Clode, P.; Vaughan, D.; Lowe, J.; Gray, D.J.; et al. Naturally occurring gold nanoparticles and nanoplates. *Geology* **2008**, *36*, 571–574. [CrossRef]
74. Hu, G.; Cao, J. Metal-containing nanoparticles derived from concealed metal deposits: An important source of toxic nanoparticles in aquatic environments. *Chemosphere* **2019**, *224*, 726–773. [CrossRef] [PubMed]
75. Cao, J. Migration mechanisms of gold nanoparticles explored in geogas of the Hetai ore district, southern China. *Geochem. J.* **2011**, *45*, e9–e13. [CrossRef]
76. Toutain, J.; Baubron, J. Gas geochemistry and seismotectonics: A review. *Tectonophysics* **1999**, *304*, 1–27. [CrossRef]
77. Etiope, G.; Martinelli, G. Migration of carrier and trace gases in the geosphere: An overview. *Phys. Earth Planet. Inter.* **2002**, *129*, 185–204. [CrossRef]
78. Malmqvist, L.; Kristiansson, K.; Kristiansson, P. Geogas prospecting—An ideal industrial application of PIXE. *Nucl. Instrum. Methods Phys. Res. Sect. B Beam Interact. Mater. At.* **1999**, *150*, 484–490. [CrossRef]
79. Cao, J.; Liu, C.; Xiong, Z.; Qin, T. Particles carried by ascending gas flow at the Tongchanghe copper mine, Guizhou Province. *Sci. China Earth Sci.* **2010**, *53*, 1647–1654. [CrossRef]
80. Cao, J.; Hu, X.; Jiang, Z.; Li, H.; Zou, X. Simulation of adsorption of gold nanoparticles carried by gas ascending from the Earth's interior in alluvial cover of the middle-lower reaches of the Yangtze River. *Geofluids* **2010**, *10*, 438–446. [CrossRef]

81. Dai, D.; Cao, J.; Lai, P.; Wu, Z. TEM study on particles transported by ascending gas flowin the Kaxiutata iron deposit, Inner Mongolia, North China. *Geochem. Explor. Env.* **2015**, *15*, 255–271. [CrossRef]
82. Cao, J.; Hu, R.; Liu, S.; Xie, G. Simulation test on migration of geogas-carrying gold nanoparticles in slope sediments. In *Mineral Deposit Research: Meeting the Global Challenge*; Springer: Berlin/Heidelberg, Germany, 2005; pp. 897–900.
83. Dilinas, J.; Jurevicius, A.; Karveliene, D. Migration forms of main chemical elements in the groundwater of the Quaternary deposits of Lithuania. *Baltica* **2009**, *22*, 123–132.
84. Barnesa, M.C.; Jeon, I.D.; Kimb, D.Y.; Huang, N.M. Generation of charged clusters during thermal evaporation of gold. *J. Cryst. Growth* **2002**, *242*, 455–462. [CrossRef]
85. Peng, Z.; Cao, J. Natural uranium-bearing nanoparticles in surface media. *Environ. Chem. Lett.* **2021**, *19*, 2713–2721. [CrossRef]
86. Luo, S.; Nie, X.; Yang, M.; Fu, Y.; Zeng, P.; Wan, Q. Sorption of differently charged gold nanoparticles on synthetic pyrite. *Minerals* **2018**, *8*, 428. [CrossRef]